Conference on Modelling Fluid Flow (CMFF'25)
The 19th International Conference on Fluid Flow Technologies
Budapest, Hungary, August 26-August 29, 2025

CAVITATION BUBBLE NEAR A WALL: SENSITIVITY TO MODELING CONDITIONS

Bo WANG[1], Zhidian YANG[2], Francesco ROMANÒ[2]

[1] Corresponding Author. Univ. Lille, CNRS, ONERA, Arts et Métiers Institute of Technology, Centrale Lille, UMR 9014 - LMFL - Laboratoire de Mécanique des Fluides de Lille - Kampé de Fériet, F-59000 Lille, France. Tel.: +33 07 81 39 91 74, E-mail: bo.wang_1@ensam.eu
[2] Univ. Lille, CNRS, ONERA, Arts et Métiers Institute of Technology, Centrale Lille, UMR 9014 - LMFL - Laboratoire de Mécanique des Fluides de Lille - Kampé de Fériet.

ABSTRACT

Cavitation near solid surfaces is a critical phenomenon due to its potential to damage materials and impair the performance of machinery such as pumps and turbines. Previous studies have employed compressible multiphase solvers to simulate the collapse of cavitation bubbles near walls, often using equivalent radius as a key parameter for validation. In this work, we aim to deepen the understanding of cavitation bubble dynamics by comparing two modeling approaches: (*i*) the Volume-of-Fluid (VOF) method with the All-Mach approach and (*ii*) the Level-Set method with Euler equations. The simulations are conducted using Basilisk and M2C, respectively, two open-source solvers that leverage adaptive meshes on the one hand and multiphysics on the other hand for high-resolution computations that can tackle complementary regimes. A novel aspect of this study is the simulation of bubble dynamics starting from the breakdown phase, which provides a more comprehensive understanding of the collapse process. Our results indicate that while the equivalent radius shows limited sensitivity to modeling conditions, the maximum wall pressure is strongly dependent on the bubble's stand-off ratio. By comparing the simulation results to experimental measurements and visualizations, we evaluate the accuracy and applicability of the two approaches under various conditions. This study provides new insights into the sensitivity of cavitation bubble collapse to modeling conditions and informs the selection of numerical methods for accurate prediction of cavitation-induced phenomena.

Keywords: bubble dynamics, bubble modeling, laser-induced cavitation

NOMENCLATURE

$max_r(P_w)$	$[MPa]$	maximum wall pressure
R_{eq}	$[mm]$	equivalent radius of bubble
$D(t_{MR})$	$[mm]$	distance from the bubble's centroid to the wall
$\max_t(R_{eq})$	$[mm]$	maximum equivalent radius of bubble

Subscripts and Superscripts

L	laser
t_{MR}	time when bubble reaches its maximum equivalent radius
eq	equivalent
r	radial direction
w	wall

1. INTRODUCTION

Cavitation refers to the formation, growth, and collapse of vapor bubbles in a liquid due to rapid changes in pressure or temperature [1, 2]. Cavitation bubbles commonly occur in hydraulic machinery such as pumps and turbines [3, 4]. On one hand, their collapse can cause erosion and vibration on solid surfaces [5]. On the other hand, cavitation can offer benefits across various fields like enhancing the drilling rate of petroleum wells [6] and performing shotless peening on metals [7]. Understanding bubble collapse near solid surfaces is therefore essential.

There is a substantial body of research dedicated to investigating cavitation bubble dynamics through experimental approaches [8, 9, 10, 11]. However, experiments face limitations such as difficulty in measuring pressure, temperature and velocity fields inside the bubble. In order to address these challenges, numerical simulations have been developed to study bubble dynamics near a solid boundary. One widely used method is the Volume-of-Fluid (VOF) method with All-Mach approach, implemented in Basilisk by [12, 13]. Simulations using this method assume predefined initial conditions, such as pressure, temperature and velocity at a given bubble size. Recently, Zhao et al. [14] employed the Level-Set method

with Euler equations using M2C solver to simulate laser-induced bubble generation, specifically focusing on pear-shaped and elongated bubble formation. Their work provides a robust framework for modeling bubble behavior and greatly advances the understanding of laser-induced bubble dynamics as they model the breakdown phase, hence the formation of the bubble.

In this work, we aim to deepen the understanding of cavitation bubble dynamics by simulating a single axi-symmetric bubble near a solid boundary. We compare the results obtained using two numerical models: the VOF method with the All-Mach approach by [13, 15] and the Level-Set method with Euler equations by [14] which will be conducted in the present study. Key metrics, such as the bubble equivalent radius and maximum wall pressure, are analyzed and validated against experimental data from [16, 17]. This comparison evaluates the accuracy and applicability of the two numerical approaches, contributing to advancements in modeling cavitation-induced phenomena.

2. PROBLEM FORMULATION

2.1. Problem description

Figure 1 illustrates the problem investigated in this work, showing an axi-symmetric vapor bubble induced by laser.

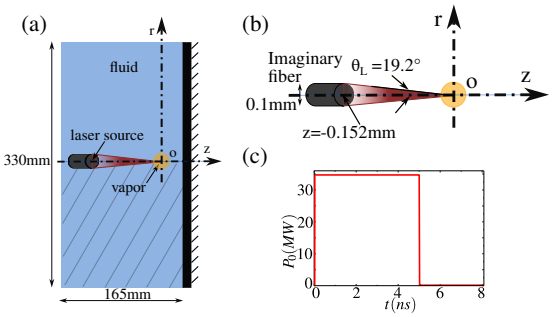

Figure 1. Schematic of laser-induced bubble generation. (a) Computational domain with axi-symmetry. (b) Geometry of the laser radiation domain. (c) Temporal profile of laser power.

In the experiment performed by [16], a Q-switched Nd: YAG laser with a wavelength of 532nm, maximum pulse energy of 200mJ and a pulse duration of 5ns was used as the energy source to induce the cavitation bubble. The experiment was carried out in a $20.3 \times 20.3 \times 20.3\ cm^3$ glass tank filled with pure water under ambient conditions: temperature $T = 293.15K$ and pressure $P = 101325Pa$.

To replicate the experimental conditions in our computational model, we employed an axi-symmetric simulation domain with radius and length of 165 mm. In our simulations, r denotes the radial coordinate. The laser, positioned outside the water tank in the experiment, is modeled as originating at $z = -0.152\ mm$, with a laser source radius of $R_L = 0.05\ mm$, and a convergence angle of $\theta_L = 19.2°$, consistent with the laboratory experiment, as shown in Fig. 1.

Computational domain size is 55 times the maximum bubble radius to avoid the impact of computational boundary on bubble shape and size by constraining its growth. The initial conditions assumed that the domain is filled with liquid water of density $\rho_0 = 0.001\ g/mm^3$, pressure $p_0 = 1atm$, and temperature $T_0 = 293.15\ K$. The flow is initially assumed at rest. In the computational model, the spatial distribution of laser intensity is simplified and treated as a step function, as shown in Fig. 1(c). The laser power increases rapidly to its peak within 0.01ns, remains constant for 5ns, and then decreases to zero over 0.02ns. In our simulation, the absorption coefficient α is set to 101222 m^{-1} for liquid water and $10^{-5}\ m^{-1}$ for the vapor. The vaporization temperature and latent heat of vaporization are specified as $T_{vap} = 373.15\ K$ and $l = 2256.4\ J/g$, respectively.

The bubble dynamics can be analyzed using two key parameters: the equivalent radius, denoted as R_{eq}, and the distance from the bubble's centroid to the solid wall, L. The stand-off ratio, expressed as

$$\gamma = \frac{D(t_{MR})}{\max\limits_{t}(R_{eq})} \tag{1}$$

quantifies the relative distance between the bubble's centroid and the wall, where t_{MR} refers to the time when the bubble reaches its maximum equivalent radius.

2.2. Governing equations

The equations, governing the compressible two-phase flows neglecting the effects of viscosity and surface tension while considering radiative heat transfer, are presented in this section. The governing equations for the conservation of mass, momentum, and energy in a compressible fluid are expressed in a conservative form as follows.

$$\frac{\partial \boldsymbol{W}(\boldsymbol{x},t)}{\partial t} + \nabla \cdot \mathcal{F}(\boldsymbol{W}) = \nabla \cdot \mathcal{G}(\boldsymbol{W}) \tag{2}$$

with

$$\boldsymbol{W} = \begin{bmatrix} \rho \\ \rho \boldsymbol{V} \\ \rho e_t \end{bmatrix}, \mathcal{F} = \begin{bmatrix} \rho \boldsymbol{V}^T \\ \rho \boldsymbol{V} \otimes \boldsymbol{V} + p\boldsymbol{I} \\ (\rho e_t + p)\,\boldsymbol{V}^T \end{bmatrix}, \mathcal{G} = \begin{bmatrix} \boldsymbol{0}^T \\ \boldsymbol{0} \\ (k\nabla T - \boldsymbol{q_r})^T \end{bmatrix}. \tag{3}$$

ρ, $\boldsymbol{V}$, p, and T denote the fluid's density, velocity, pressure, and temperature, respectively. The total energy per unit mass, e_t, is defined as

$$e_t = e + \frac{1}{2}|\boldsymbol{V}|^2 \tag{4}$$

where e represents the fluid's internal energy per unit mass. k is the thermal conductivity coefficient, set to 0.5576 W/mK for liquid and 0.02457 W/mK for vapor. $\boldsymbol{q_r}$ refers to the radiative heat flux induced by the laser. To close the governing equations (2), a complete equation of state (EoS) for each phase, including a temperature equation, is required. In this study, the Noble-Abel stiffened gas ($NASG$) equations are

employed as the pressure and temperature equation [18] for both phases. Specifically,

$$p_I(\rho, e) = (\gamma_I - 1)\frac{e - q_I}{\frac{1}{\rho} - b_I} - \gamma_I p_{cI} \tag{5}$$

$$T_I(\rho, e) = \frac{\gamma_I}{c_{pI}}\left(e - q_I - \left(\frac{1}{\rho} - b_I\right)p_{cI}\right) \tag{6}$$

in which the subscript $I \in \{0, 1\}$ identifies the liquid (0) and vapor (1) phases. For each phase, γ, p_c, q and b are constant parameters that characterize its thermodynamic properties. c_p denotes the specific heat capacity at constant pressure, assumed to be a constant. The values of these parameters and other related thermodynamic properties are adopted from Zein et al. [19] and summarized in Table 1.

Table 1. NASG EoS parameters and thermodynamic properties for liquid and vapour phase.

Parameter	Units	Value
c_{p0}	J kg^{-1} K^{-1}	7094.593
γ_0	–	2.057
p_{c0}	Pa	1.066×10^9
b_0	m^3 kg^{-1}	0
q_0	J kg^{-1}	-1994.674×10^3
c_{p1}	J kg^{-1} K^{-1}	1592.4
γ_1	–	1.327
p_{c1}	Pa	0
b_1	m^3 kg^{-1}	0
q_1	J kg^{-1}	1995×10^3

The laser radiation equation is derived based on energy conservation, taking into account the assumptions that the laser radiation dominates over the black-body radiation and that the laser propagates in a fixed direction with a certain wavelength [14].

$$\nabla \cdot (L\boldsymbol{s}) = \nabla L \cdot \boldsymbol{s} + (\nabla \cdot \boldsymbol{s})L = -\alpha(I)L \tag{7a}$$

$$\boldsymbol{q}_r = L\boldsymbol{s} \tag{7b}$$

where $s = s(x)$ denotes the direction of the laser propagation, which is constant only when the beam is parallel. The spatial variable x refers to the position on the surface of the laser fiber, where the initial laser radiance used to induce the vapor bubble is calculated, and L represents the laser radiance, which can be calculated for uniform beam as:

$$L = \frac{P_0(1 + \cos\theta_L)}{\pi r^2} \tag{8}$$

2.3. Numerical schemes

In this section, we present a summary of the numerical schemes used, and we refer to Zhao et al. [14] for a detailed description. The above governing equations are solved using a finite volume method based on exact multiphase Riemann problem solver. The vapor-liquid interface is tracked by the level set method and the phase transition process is accomplished when the intermolecular potential energy in the liquid phase reaches the latent heat.

In the current study, we do not model the laser fiber as a fixed boundary interacting with the vapor since the bubble in our case is free-floating without interaction with the fiber.

3. SPATIAL CONVERGENCE STUDY

3.1. The global influence of mesh resolution

In this section, the influence of global mesh refinement is investigated to identify an optimal mesh size that ensures convergence in the bubble's generation simulated using M2C. We refer to Yang et al. [17] for a detailed grid convergence study for Basilisk.

As shown in Figure 2(a), the axi-symmetric computational domain is $330mm \times 165mm$. Since the bubble induced by laser has an experimental radius of approximately 2.7mm, a region of $9mm \times 8mm$ (indicated by a cyan dashed box) is designated with finer mesh resolution than the surrounding area, as illustrated in Fig. 2(b). This region, larger than the maximum bubble radius, ensures that the bubble can grow and collapse under a consistent mesh refinement. The red area highlights the location where the bubble will evolve.

At first, only the mesh size within this designated region is varied, while the mesh outside remains unchanged. Seven cases for $\gamma = 1.82$ are examined, with minimum cell size from $\Delta x = 4.5 \times 10^{-6}$m to $\Delta x = 10^{-5}$m.

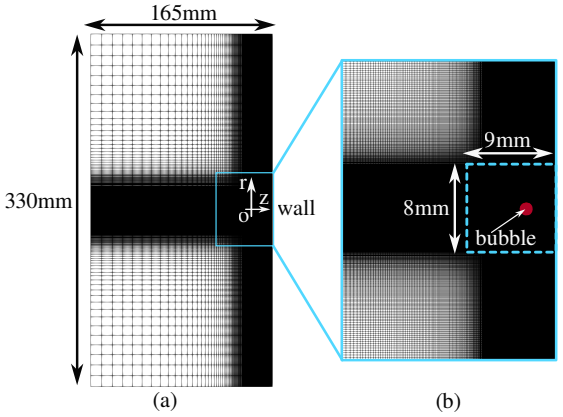

Figure 2. Global mesh distribution

In Figure 3, it can be observed that all cases exhibit a rapid expansion of the bubble in the first 270-300 μs, reaching a maximum radius between 2.6mm and 2.8mm, which corresponds well with the experimentally measured radius of approximately 2.7mm. The maximum bubble radius tends to converge as the mesh is refined. Minimum cell sizes finer than $\Delta x = 5 \times 10^{-6}$m show less variability in the maximum radius and collapse time. Besides, in Figure 4, similar to the bubble radius, the pressure peak at the wall reaches a convergence at $\Delta x = 5 \times 10^{-6}$m. Therefore, based on both the bubble radius and the

pressure peak, $\Delta x = 5 \times 10^{-6}$m is an optimal choice for balancing computational cost and accuracy.

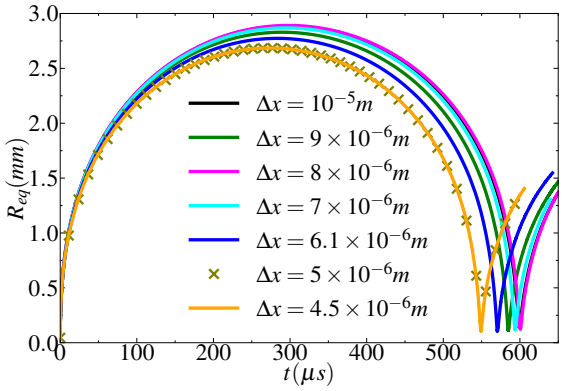

Figure 3. Evolution of bubble radius obtained with different computational meshes. The minimum cell size is reported in the legend.

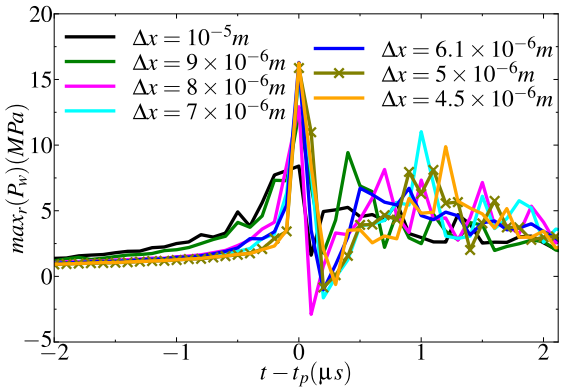

Figure 4. Evolution of pressure at wall obtained with different computational meshes. The minimum cell size is reported in the legend.

3.2. The local influence of mesh resolution

After determining the optimal global mesh size, we further study the sensitivity of bubble nucleation to local spatial resolution. Since our model initially assumes a domain entirely filled with liquid, a bubble is generated as part of the simulation mesh element. Suppose we do not maintain a consistent initial mesh near the region of bubble nucleation. In that case, each simulation will generate different initial bubbles due to the varied spatial resolution, leading to non-comparable results. This makes it imperative to fix the initial mesh to ensure repeatability and consistency across different simulations.

To further validate our numerical approach, three simulations are carried out: **(a)** a first simulation with a fixed extra-fine region at nucleation site whose cell size is Δx=5×10^{-6}m, while $10^{-5}m$ is used elsewhere within the cyan dashed box of fig. 2, **(b)** a second simulation with uniform cell size Δx=5×10^{-6}m within the cyan dashed box of fig. 2, and **(c)** a third simulation with uniform cell size Δx=10^{-5}m within the cyan dashed box of fig. 2. The equivalent bubble radius during the first $45\mu s$ after bubble generation is depicted in figure 5. We observe that the initial bubble generation is highly sensitive to spatial resolution around the nucleation site. Specifically, the difference between the black curve(with a uniform mesh size of 10^{-5}m throughout the domain) and the magenta curve(with a refined mesh size of 5×10^{-6}m in the nucleation region and 10^{-5}m elsewhere) is significantly larger than the difference between cyan and magenta curves. This observation confirms the necessity of fixing the initial mesh around the bubble nucleation site to ensure consistent results.

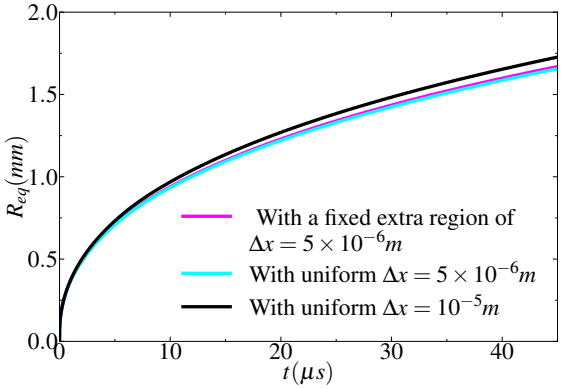

Figure 5. Influence of local mesh refinement at nucleation site.

To make sure that the bubble will be generated under identical initial conditions, we fix the mesh resolution in the region of $0.4mm \times 0.6mm$ near the bubble nucleation site, denoted as Ω0. Specifically, the mesh size is set to 5×10^{-6}m within Ω0 for the first 200 time steps, as Figure 6 . This mesh size was determined to be optimal in the previous section.

Outside this space (Ω1), the mesh size can vary, but the bubble will always start within the extra fine mesh in Ω0. This setup allows for reliable convergence studies, as the bubble's initial formation is consistent across simulations, regardless of the coarser mesh outside Ω0.

Fig. 6 illustrates this mesh configuration, highlighting the denser mesh region around the nucleation site and the coarser mesh outside of it.

To determine the optimal mesh size in the region Ω1, three cases for $\gamma = 1.82$ are considered, with different mesh sizes: $\Delta x = 10^{-5}$m, 2×10^{-5}m, 5×10^{-6}m. In particular, we focus on the evolution of the bubble radius and the pressure exerted at the wall. From Figure 7, all simulations capture the general trend of bubble growth and collapse. The bubble expands and then collapses, following the same qualitative behavior as the experimental measurements. The mesh resolution of $\Delta x = 10^{-5}$m shows a better agreement with the experimental results, reaching a

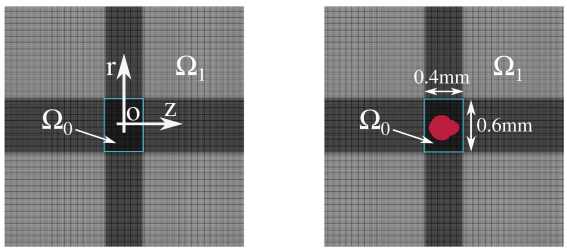

Figure 6. Local mesh distribution near the bubble nucleation site. (a) t=0s. (b) t=10^{-7}s. The red area within Ω_0 represents the bubble right after its nucleation.

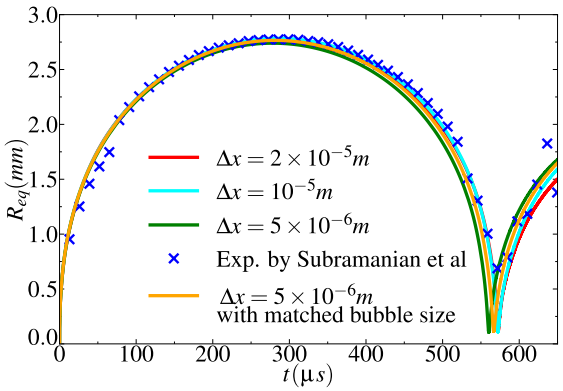

Figure 7. Comparison of radius between experiment and simulation.

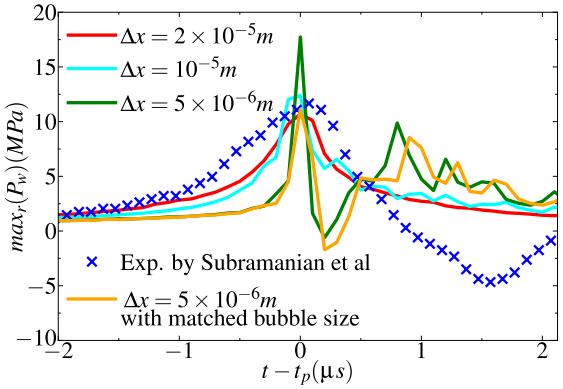

Figure 8. The sensitivity of wall pressure to mesh size.

maximum radius of 2.7 mm which matches well the experimental results. Besides, in Figure 8, the simulation with $\Delta x = 10^{-5}$m exhibits a relative error of 1.3% in the timing of the peak pressure and 6% in the peak pressure value, compared to the experimental measurements.

A notable feature regarding maximum wall pressure for Δx $=5 \times 10^{-6}$m is found to be approximately 17MPa (see green line in fig. 8). This pressure peak is significantly higher than what observed experimentally (see blue crosses in fig. 8) and speculate that it is due to inaccuracies on the prediction of the bubble size rather than to mesh resolution. To verify our assumption, an additional simulation was conducted using the same mesh resolution of Δx $=5 \times 10^{-6}$m but with a 20% higher absorption coefficient. This adjustment led to a 1% increase in the numerical maximum bubble size, matching the experimental measurements by [16] (see orange line in fig. 7). The wall pressure is highly sensitive to the collapse dynamics. As the bubble grows slightly larger, its collapse becomes significantly less sharp due to a reduced collapse velocity and lower compression of the surrounding fluid. This deceleration diminishes the intensity of the pressure wave generated during collapse, and consequently, the impact on the wall is reduced. The resulting pressure peak for the size-matched simulation is now in good agreement with the experiments, as shown by the orange line in fig. 8. This confirms that Δx $= 5 \times 10^{-6}$m gives similar results to $\Delta x = 10^{-5}$m once the bubble dynamics are properly matched with the experiment data. Therefore, $\Delta x = 10^{-5}$m is chosen as the converged mesh size for region Ω1, ensuring accurate and efficient simulations in the following studies.

In conclusion, a spatial convergence study has been conducted and we identified an optimal mesh size of $\Delta x = 5 \times 10^{-6}$m within Ω0 and 10^{-5}m within Ω1 to conduct the following simulations.

4. RESULTS

In this study, three γ are considered, i.e. $\gamma \approx 1$, 1.6, 2.2, in order to investigate three conceptually different cavitation regimes ([16]). A single bubble near a solid wall is modeled by two different approaches. Firstly, we simulate a cavitation bubble initialized at rest. The corresponding simulations are carried out using two numerical solvers, namely Basilisk [12] and M2C [14]. As the two solvers employ different numerical methods and discretization approaches, this preliminary comparison will allow us to single out the discrepancies in the numerical simulations that are due to the numerical solver. Hence, we compare them in terms of the time evolution of (*i*) the equivalent bubble radius (R_{eq}, i.e. the radius of a fictitious spherical bubble with the same volume), and (*ii*) the maximum wall pressure ($\max_r(P_w)$).

A second part of our investigation includes the laser generation and the first collapse. In this second part, we use the sole M2C solver, owing to its multiphysics capabilities to simulate a laser-induced bubble from the generation point. By comparing the equivalent radius and the maximum wall pressure between our simulations and the experimental measurements by [16], we will discuss the limitations of simulating a cavitation bubble starting from rest.

4.1. A bubble from rest

This section examines the dynamics of a bubble near a wall assuming that the bubble has been initialized at rest starting from its maximum size. The initial bubble temperature is set to be $T_{G,0}/T_{L,0}$=0.826. The initial pressure ratio between outside and inside the bubble is specified to be $P_{G,0}/P_{L,0}$=1/50. Two solvers are here compared, i.e. M2C and Basilisk, making sure that the simulations have consistent initial configurations and converged mesh resolution. The selected stand-off ratios are γ=1.049, 1.537, 2.152, as for such three stand-off ratios we can initialize the bubble shape using the fitting of [17].

As illustrated in Figure 9, both equivalent radius and collapse time predicted by Basilisk and M2C show a strong agreement. The deviation between the two numerical solvers remains within 5% for the collapse time. Furthermore, the collapse times predicted by both solvers are within the range reported in the experiments by [16, 17]. We further stress that both solvers reproduce the trend observed in the experiments, i.e. $t_c \downarrow$ for $\gamma \uparrow$.

Regarding the maximum wall pressure $\max_r(P_w)$, as shown in Fig. 10, both solvers display a similar trend across all γ. However, M2C tends to predict a sharper increase in $\max_r(P_w)$ in time near the pressure peak time t_p. As γ increases from 1.049 to 2.152, both solvers predict a decrease in the peak pressure.

A significant deviation is observed for γ = 1.049, with M2C predicting a pressure peak approximately 50% higher than Basilisk. Furthermore, an oscillatory behavior appears in the M2C result, which is absent in Basilisk. This highlights the sensitivity of $\max_r(P_w)$ for $\gamma \approx 1$. This discrepancy in pressure peak and the oscillatory behavior may stem from differences in interface capturing methods (VOF vs Level-Set method), as well as variations in discretization schemes. In particular, the nonphysical behavior observed with the Level Set method may be related to its frequent re-initialization process inherent to the method, which can shift the interface position. This becomes especially problematic near the wall, where such shifts can locally violate pressure continuity and lead to non-physical pressure peaks and oscillations. In contrast, for γ = 1.537 and 2.152, the relative error significantly reduces to a range of 5% to 8% in pressure peak.

In conclusion, both M2C and Basilisk can effectively simulate the dynamics of a bubble initially at rest near a wall. While the equivalent radius and collapse time show minimal sensitivity to the modeling approaches, the maximum wall pressure exhibits a stronger variability, particularly for $\gamma \approx 1$. A detailed comparison with the modeling approach including laser generation must therefore focus primarily on the pressure quantification, rather than on interfacial indicators.

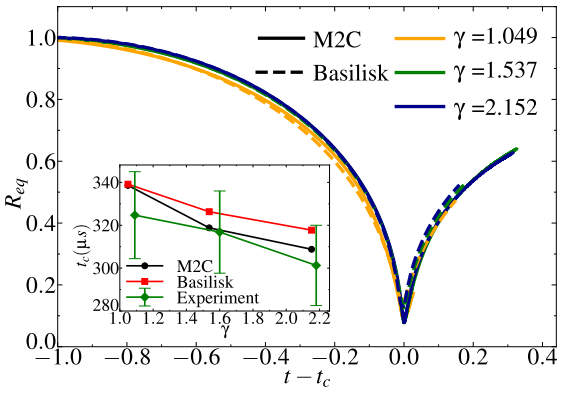

Figure 9. Bubble equivalent radius and collapse time: Comparison between the two numerical solvers for three stand-off ratios. The inset shows the numerical collapse times for the three stand-off ratios, compared with the experimental measurements by [16, 17].

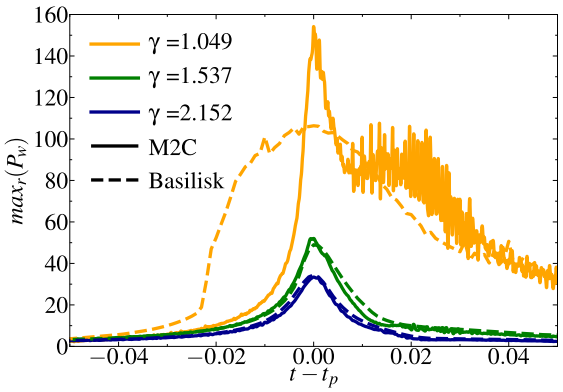

Figure 10. Maximum wall pressure: Comparison between the two numerical solvers for three stand-off ratios.

4.2. A bubble from laser generation

In this section, three slightly different γ are selected, i.e., γ= 1.07, 1.68, 2.18, as they correspond to the stand-off ratios reproduced in the laser-induced cavitation experiments of [16]. We will now simulate bubble generation thanks to the capacitive phase-change approach implemented in M2C.

As illustrated in Figure 11, the maximum wall pressure predicted by the simulation generally matches well with the experimental measurements, although a significant deviation of 34% for γ=1.68 in the pressure peak is observed. This discrepancy is likely attributed to the difference in the equivalent radius and interfacial dynamics between experimental results and the simulation, as shown in Figure 12. For γ=1.07 and for γ=2.18, we observe that the relative error is considerably smaller, around 5% and 2% in pressure peak, respectively. This minimal deviation can also be explained by the nearly-perfect match between the bubble's equivalent radius evol-

ution in M2C simulation and experimental data for these two γ.

Figure 13 shows the comparison in wall pressure among the simulation of bubble initially at rest implemented with both M2C and Basilisk, the simulation of bubble from generation using M2C, and experimental measurements. The results indicate that simulating the bubble generation provides better agreement with the experiments and simulations initiated from rest, regardless of the numerical approach used, largely underestimate the pressure peak at $\gamma > 1$. This highlights the importance of including the memory of the formation and expansion phases in the bubble dynamics simulations.

To further reinforce the significance of modeling the entire bubble evolution from the breakdown phase, two additional cases for $\gamma \approx 1.6$ were simulated with M2C: (*i*) one including only the expansion and collapse phases, initialized with a small radius of 0.16 mm and high internal pressure and temperature ($P_{G,0}/P_{L,0} = 3225$, $T_{G,0}/T_{L,0} = 33.67$); (*ii*) another considering only the collapse phase, starting from the maximum bubble size of 2.7mm with initial pressure and temperature corresponding to a bubble from rest (i.e. $P_{G,0}/P_{L,0} = 1/50$, $T_{G,0}/T_{L,0} = 0.826$), as shown in Figure 14 and 15. These results clearly show that including the bubble breakdown phase provides the best agreement with experimental measurements by [16], while simulations that model only the expansion and collapse phases perform better than those starting solely from the maximum radius, which are the least accurate.

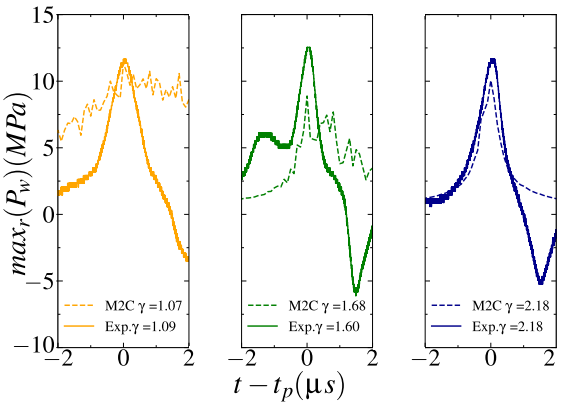

Figure 11. Maximum wall pressure: Comparison between simulations (dashed lines) and experiments by [16] (solid lines).

5. CONCLUSION

Simulations of bubbles from rest, implemented using M2C and Basilisk, demonstrate strong agreement in predicting the equivalent radius and collapse time, with deviations between the two solvers remaining within 5%. Both methods accurately capture the trend of decreasing collapse time as γ increases, and the simulated results match well with

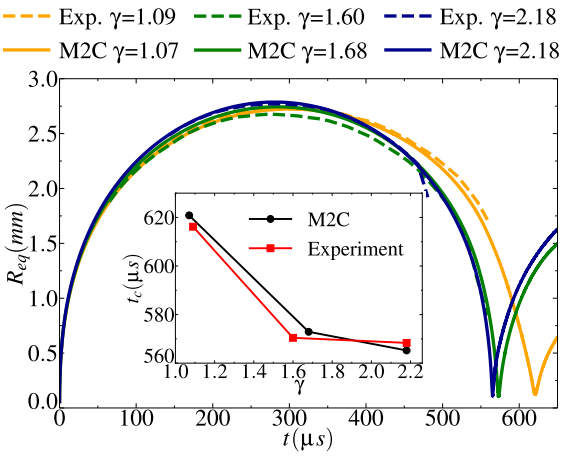

Figure 12. Evolution of R_{eq} simulated by M2C (solid lines) and measured experimentally by [16] (dashed lines), together with the collapse time reported in the inset.

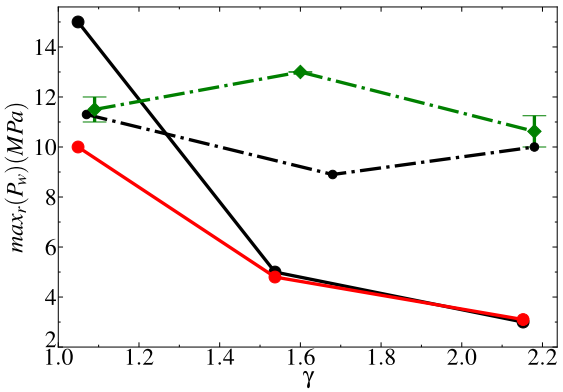

Figure 13. Comparison of maximum wall pressure. The solid lines denote simulations from rest carried out using M2C (solid black line) and Basilisk (solid red line). The black dashed-dotted line refers the M2C simulations including the laser-generation of the cavitation bubble, while the green dashed-dotted line refers to the experiments by [16].

experimental measurements for these metrics. However, the maximum wall pressure ($\max_r(P_w)$) shows greater sensitivity to the modeling approach, particularly at lower γ. For $\gamma \approx 1$, a significant discrepancy of approximately 50% is observed between both solvers, highlighting the influence of differences in interface capturing methods (VOF vs Level-Set method) and numerical discretizations.

Simulations of bubble from its nucleation, conducted with M2C, achieve better agreement with experimental results compared to those started with the bubble at rest. By incorporating the formation and expansion phases of the bubble, the simulation provides more accurate predictions of maximum wall pressure and a comprehensive understanding of

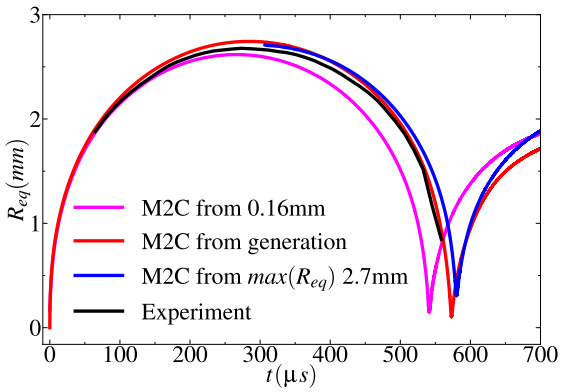

Figure 14. Comparison of R_{eq} for $\gamma \approx 1.6$ obtained from M2C simulations initialized at different starting points and measured experimentally by [16].

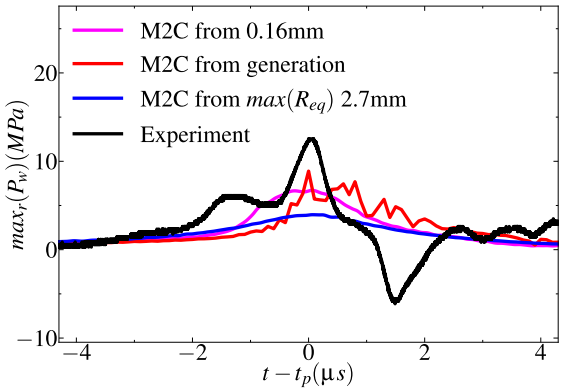

Figure 15. Comparison of $max_r(P_w)$ for $\gamma \approx 1.6$ obtained from M2C simulations initialized at different starting points and measured experimentally by [16].

bubble collapse. For $\gamma \approx 1$ and $\gamma \approx 2.2$, relative errors in wall pressure peak between simulation and experiment are minimal, at approximately 5% and 2%, respectively. However, for $\gamma \approx 1.6$, a significant deviation of 34% in pressure peaks was observed. This discrepancy is attributed to differences in the evolution of bubble radius and interfacial dynamics between the simulation and experiment, as evidenced by the radius evolution analysis.

Overall, simulations of bubbles from generation exhibit superior accuracy in predicting experimental results compared to those from rest. While both modeling approaches are effective in capturing key bubble dynamics such as collapse time and equivalent radius, the inclusion of the formation and expansion phases in the simulation process enhances the predictive capability for maximum wall pressure. These findings underscore the sensitivity to the initialization modeling assumptions and further studies will be aimed to identify the initial conditions capable of simulating the bubble dynamics without necessarily including the bubble generation.

ACKNOWLEDGEMENTS

This work has been financially supported by the Chinese Scholarship Council (CSC) for B. Wang (student number 202206240030) and Z. Yang (student number 202008310185).

REFERENCES

[1] Brennen, C. E., 2014, *Cavitation and bubble dynamics*, Cambridge university press.

[2] Franc, J.-P., and Michel, J.-M., 2006, *Fundamentals of cavitation*, Vol. 76, Springer science & Business media.

[3] Cristofaro, M., Edelbauer, W., Koukouvinis, P., and Gavaises, M., 2020, "A numerical study on the effect of cavitation erosion in a diesel injector", *Applied Mathematical Modelling*, Vol. 78, pp. 200–216.

[4] Balz, R., Nagy, I. G., Weisser, G., and Sedarsky, D., 2021, "Experimental and numerical investigation of cavitation in marine Diesel injectors", *International Journal of Heat and Mass Transfer*, Vol. 169, p. 120933.

[5] Arndt, R. E., 1981, "Cavitation in fluid machinery and hydraulic structures", *Annual Review of Fluid Mechanics*, Vol. 13 (1), pp. 273–326.

[6] Gensheng, L., Zhonghou, S., Changshan, Z., Debin, Z., and Hongbing, C., 2005, "Investigation and application of self-resonating cavitating water jet in petroleum engineering", *Petroleum science and technology*, Vol. 23 (1), pp. 1–15.

[7] Soyama, H., Chighizola, C. R., and Hill, M. R., 2021, "Effect of compressive residual stress introduced by cavitation peening and shot peening on the improvement of fatigue strength of stainless steel", *Journal of Materials Processing Technology*, Vol. 288, p. 116877.

[8] Zhao, B., and Coutier-Delgosha, O., 2023, "The impacts of material acoustic impedance and thickness on single laser-induced bubble dynamics and determining factors in resulting pressure", *Physics of Fluids*, Vol. 35 (10), p. 103303, URL `https://doi.org/10.1063/5.0168349`, `https://pubs.aip.org/aip/pof/article-pdf/doi/10.1063/5.0168349/18151383/103303_1_5.0168349.pdf`.

[9] Zhang, J.-y., Du, Y.-x., Liu, J.-q., Sun, Y.-r., Yao, Z.-f., and Zhong, Q., 2022, "Experimental and numerical investigations of the collapse of a laser-induced cavitation bubble near a solid wall", *Journal of Hydrodynamics*, Vol. 34 (2), pp. 189–199.

[10] Ren, X., He, H., Tong, Y., Ren, Y., Yuan, S., Liu, R., Zuo, C., Wu, K., Sui, S., and Wang, D., 2016, "Experimental investigation on dynamic characteristics and strengthening mechanism of laser-induced cavitation bubbles", *Ultrasonics sonochemistry*, Vol. 32, pp. 218–223.

[11] Zhang, Y., Xie, X., Zhang, Y., and Du, X., 2019, "Experimental study of influences of a particle on the collapsing dynamics of a laser-induced cavitation bubble near a solid wall", *Experimental Thermal and Fluid Science*, Vol. 105, pp. 289–306.

[12] Saade, Y., Lohse, D., and Fuster, D., 2023, "A multigrid solver for the coupled pressure-temperature equations in an all-Mach solver with VoF", *Journal of Computational Physics*, Vol. 476, p. 111865, URL https://www.sciencedirect.com/science/article/pii/S0021999122009287.

[13] Fuster, D., and Popinet, S., 2018, "An all-Mach method for the simulation of bubble dynamics problems in the presence of surface tension", *Journal of Computational Physics*, Vol. 374, pp. 752–768, URL https://www.sciencedirect.com/science/article/pii/S0021999118305187.

[14] Zhao, X., Ma, W., and Wang, K., 2023, "Simulating laser-fluid coupling and laser-induced cavitation using embedded boundary and level set methods", *Journal of Computational Physics*, Vol. 472, p. 111656, URL https://www.sciencedirect.com/science/article/pii/S0021999122007197.

[15] Saade, Y., Lohse, D., and Fuster, D., 2023, "A multigrid solver for the coupled pressure-temperature equations in an all-Mach solver with VoF", *Journal of Computational Physics*, Vol. 476, p. 111865.

[16] Subramanian, R. K., Yang, Z., Romanò, F., and Coutier-Delgosha, O., 2024, "Bubble collapse near a wall. Part 1: An experimental study on the impact of shock waves and microjet on the wall pressure", URL https://arxiv.org/abs/2408.03479, 2408.03479.

[17] Yang, Z., Subramanian, R. K., Wang, B., Coutier-Delgosha, O., and Romanò, F., 2025, "Bubble collapse near a wall: A numerical study on the impact of physical mechanisms for a bubble initially at rest", *submitted*.

[18] Métayer, O. L., Saurel, R., Métayer, O. L., and Saurel, R., 2016, "The Noble-Abel Stiffened-Gas equation of state", Vol. 046102, URL http://dx.doi.org/10.1063/1.4945981.

[19] Zein, A., Hantke, M., and Warnecke, G., 2013, "On the modeling and simulation of a laser-induced cavitation bubble", *International Journal for Numerical Methods in Fluids*, Vol. 73, pp. 172–203.